A LETTERS JOURNAL EXPLORING THE FRONTIERS OF PHYSICS

OFFPRINT

Shear thickening in highly viscous granular suspensions

Qin Xu, Sayantan Majumdar, Eric Brown and Heinrich M. Jaeger

EPL, **107** (2014) 68004

A Letters Journal Exploring the Frontiers of Physics

September 2014

EPL, **107** (2014) 68004 www.epljournal.org
doi: 10.1209/0295-5075/107/68004

Shear thickening in highly viscous granular suspensions

Qin Xu[1,2], Sayantan Majumdar[2], Eric Brown[3] and Heinrich M. Jaeger[1,2]

[1] *Department of Physics, University of Chicago - Chicago, IL 60637, USA*
[2] *James Franck Institute, University of Chicago - Chicago, IL 60637, USA*
[3] *Department of Mechanical Engineering and Materials Science, Yale University - New Haven, CT 06520, USA*

received 18 June 2014; accepted in final form 1 September 2014
published online 19 September 2014

PACS 83.60.Rs – Shear rate-dependent structure (shear thinning and shear thickening)
PACS 47.57.E- – Complex fluids and colloidal systems: Suspensions
PACS 83.80.Hj – Suspensions, dispersions, pastes, slurries, colloids

Abstract – We experimentally investigate shear thickening in dense granular suspensions under oscillatory shear. Directly imaging the suspension-air interface, we observe dilation beyond a critical strain γ_c and the end of shear thickening as the maximum confining stress is reached and the contact line moves. Analyzing the shear profile, we extract the viscosity contributions due to hydrodynamics η_h, dilation η_c and sedimentation η_g. While η_g governs the shear thinning regime, η_h and η_c together determine the shear thickening behavior. As the suspending liquid's viscosity varies from 10 to 1000 cSt, η_h is found to compete with η_c and soften the discontinuous nature of shear thickening.

Introduction. – Dense suspensions can increase their viscosity under rapid shear; *i.e.*, they exhibit shear thickening (ST) [1–11]. To understand the origin of this ST transition, several mechanisms have been proposed. A hydro-cluster picture ascribes mild, continuous thickening to particle groups formed by viscous hydrodynamic interactions [12–14]. Dense granular suspensions can exhibit a much stronger shear thickening, so that the viscosity can increase discontinuously with the shear rate as a critical packing fraction is approached [15–17]. Recent works have related this to frictional particle interactions and dilation [2,3,18,19], similar to dry granular materials. In this scenario, the Laplace pressure due to surface tension at the suspension-air interface keeps the suspension contained. Since granular systems prefer to dilate when made to flow, the normal stress and, subsequently, the friction between suspension and shear plate dramatically increases beyond a certain applied stress. Thus, the measured flow resistance shoots up as long as dilation is counteracted by confinement.

In this granular mechanism, the frictional stress between solid particles is the dominant contributor to ST. The suspending liquid mainly acts as a boundary constraint to prevent expansion. Nevertheless, viscous hydrodynamic interactions, as another dissipation mechanism, still exist in the bulk [4,8,9], and lubrication and viscous drag could become significant when the suspending liquid is highly viscous. So far, however, an experimental characterization of how the hydrodynamics couples with dilation and affects the shear thickening of nearly jammed granular suspensions has been lacking.

In this letter, we address this issue by investigating dense granular suspensions across a wide range of suspending liquid viscosities. The suspended particles are chosen to be sedimenting so that the friction between particles can provide a known scaling for the onset stress of shear thickening [5]. To finely control the relative displacement between particles, oscillatory shear with controlled amplitude is applied to the samples. Measuring both global rheology and local shear profile, we quantitatively extract the contributions from viscous hydrodynamics, confinement ("frustrated dilation") and sedimentation to the measured flow resistance.

Experimental setup and protocol. – Dense granular suspensions were prepared by adding ZrO_2 particles ($\rho_{ZrO_2} = 3.92\,\mathrm{g/ml}$, $200 \pm 10\,\mu\mathrm{m}$) and glass beads ($\rho_{\mathrm{glass}} = 2.55\,\mathrm{g/ml}$, $22 \pm 5\,\mu\mathrm{m}$) to silicone oils, with packing fraction $\phi \approx 54$–55%. The particles were too large to exhibit measurable Brownian motion. Rheological measurements were performed in an Anton Paar rheometer with a 25 mm diameter parallel-plate geometry allowing us to conveniently access the global normal force. The gap size d was varied from 1 to 2 mm. The top plate was set to apply a sinusoidal strain, $\gamma = \gamma_0 \sin(\omega t)$, to the sample. We fit the measured shear stress to an oscillating waveform

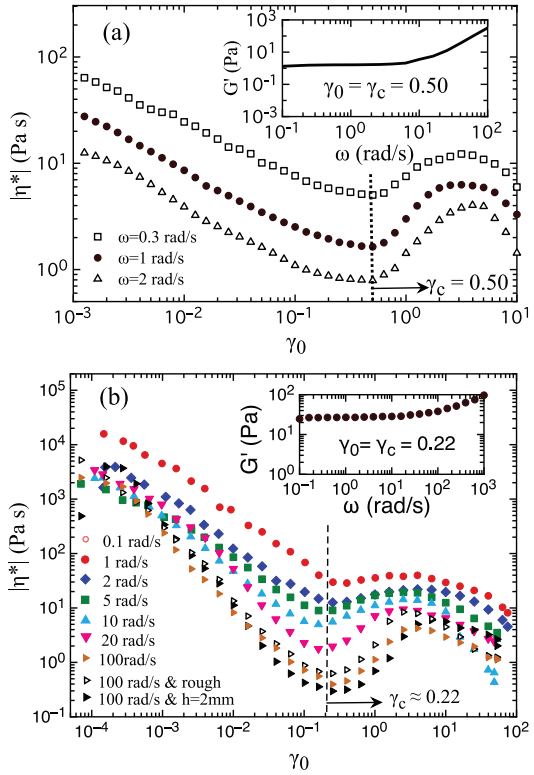

Fig. 1: (Color online) Rheological characterization of the viscosity $|\eta^\star|$ as a function of the applied oscillatory strain amplitude γ_0 for (a) ZrO_2 particles (200 μm) in 350 cSt silicone oil and (b) glass spheres (22 μm) in 100 cSt silicone oil at different oscillation frequencies ω. Shear thickening starts at $\gamma_c \approx 0.50$ (a), and $\gamma_c \approx 0.22$ (b), independently of ω. Insets: storage modulus $G'(\omega)$ *vs.* ω measured by fixing γ_0 at γ_c.

to obtain its the amplitude τ_0 [20–22]. The magnitude of the complex viscosity is defined as $|\eta^\star| = \tau_0/(\omega\gamma_0)$, the ratio of shear stress amplitude to applied strain rate. Before each measurement, the sample was pre-sheared to ensure repeatability. We used Vision Research Phantom V9 cameras with a macro lens (Nikon Micro 105 mm) to capture the dilation process. The frame rate was kept at 300 fps with spatial resolution $\sim 12\,\mu$m/pixel. The samples were illuminated from the front by two white-light sources (12 V/200 W, Dedolight).

Rheology. – We first focus on a ZrO_2 suspension with oil viscosity of 350 cSt. The rheology is quantified by ramping the strain amplitude γ_0 while keeping ω fixed in each round of measurement (fig. 1). At the beginning of a ramp, $|\eta^\star|$ decreases with γ_0, that is, the samples shear-thin. Beyond a critical strain $\gamma_c \approx 0.50$, $|\eta^\star|$ starts to increase with γ_0, indicating shear thickening. Our oscillatory measurements show that shear thickening will not occur until two neighboring particles experience relative displacement $a\gamma_c$. As previously observed by Fall *et al.* [23], the value of γ_c does not change with ω. To rule out slip [24], we performed the tests varying gap size and plate roughness (with a sand paper). No shift of γ_c was observed.

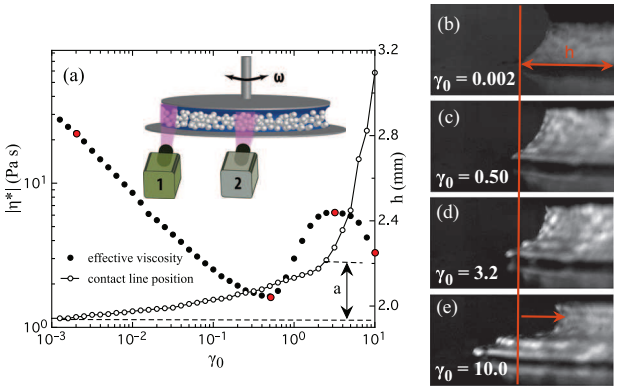

Fig. 2: (Color online) Movement of the suspension-air interface. (a) Viscosity $|\eta^\star|$ and radial distance, h, to the outer edge of the suspension as a function of the applied strain amplitude γ_0. Inset: sketch of the setup. Cameras 1 and 2 are used for imaging the interface and the velocity profile. (b)–(e) Images of the suspension boundary at specific γ_0 values, which are also displayed as red dots in (a). The vertical red line indicates the initial contact line position between suspension and substrate.

The onset of ST at γ_c can be related to a stress scale. In oscillatory measurements, the onset stress is $\tau_{min} = \omega\gamma_c|\eta^\star|_{\gamma=\gamma_c}$. From each flow curve in fig. 1, we calculate τ_{min} and find that the suspension has $\tau_{min} \approx 0.75$ Pa, independently of ω. At the same time, the elastic modulus $G'(\omega)$ stays around $G'_c \approx 1.4$ Pa for ω from 0.1 to 10 rad/s (inset of fig. 1(a)). Since the measured loss modulus is much smaller (~ 0.1 Pa) in the same regime, the critical strain γ_c is given by τ_{min}/G'_0 (≈ 0.5).

Qualitatively similar results were also found for suspensions of small glass beads (22 μm, see fig. 1(b)). A frequency-independent onset strain, $\gamma_c(\approx 0.22)$, is also measured, confirming that, while varying the relative ratio of the gap to a particle size from about one-hundred to ten, the shear thinning and thickening behaviors remain unchanged [25].

Imaging of the interface and shear profile. – To quantify the particle dynamics and confirm the occurrence of dilation in the suspensions, we image the liquid-air interface while the strain is ramped up. For these experiments, the ZrO_2 suspensions with their larger diameters were used in order to be able to track individual particles. The solid points in fig. 2(a) show the rheological curve at $\omega = 1$ rad/s. Figures 2(b)–(e) present an image sequence of the interface evolution. At $\gamma_0 = 0.002$, particles are completely contained in the liquid and no protrusions are observed at the surface (see fig. 2(b)). As γ_0 approaches $\gamma_c \approx 0.50$, the shape of individual particles becomes visible (fig. 2(c)). The local deformation of the interface can also be seen from the change of image brightness.

The vertical red line in fig. 2 represents the initial position of the contact line between suspension and substrate. By tracking the outermost edge of suspension on the substrate, we plot the radial contact line position h against

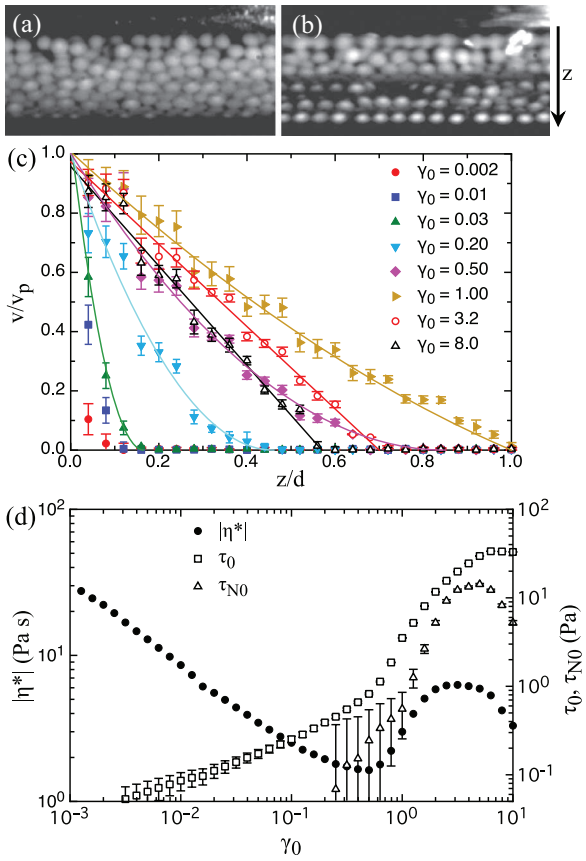

Fig. 3: (Color online) Shear profile and stress scales. (a), (b): front-view images of 54% ZrO_2 (200 μm) in 350 cSt silicone oil at $\gamma_0 = 1.0$ and 8.0. (c) For the ZrO_2 suspension shown in fig. 2, the time-averaged velocity profiles v/v_p, normalized by the speed of the top plate, are plotted against the normalized depth z/d for different γ_0. Here $z = 0$ corresponds to the top plate. The data points are obtained from PIV and the solid lines are fits to eqs. (2)–(4). (d) Shear (hollow squares) and normal stress (hollow triangles) amplitude together with the viscosity curves (solid circles).

γ_0 in fig. 2(a) (hollow circles). At $\gamma_0 = 3.2$, the edge has moved out about one particle diameter a and $|\eta^\star|$ starts to turn down (fig. 2(d)). Thus, shear thickening stops when a full particle has been pushed out. This implies that the maximum confining stress from surface tension has been reached [16]. As a result, at higher strains or shear rates, the suspension thins, *i.e.* $|\eta^\star|$ decreases and approximately scales as $\sim 1/\gamma_0$. With continuing increase of γ_0, the bottom portion of the suspension is further expanded (fig. 2(e), $\gamma_0 = 10.0$). At the same time, the upper portion retracts as well (red arrow in fig. 2(e))[1]. The reduction of contact area can provide up to 15% uncertainty to the viscosity beyond the peak point. Qualitatively similar results were found for the 22 μm glass spheres, although here we could not resolve individual particles.

To extract the shear profile, a second camera was placed right in front of the suspension. Figures 3(a) and (b) show typical images at $\gamma_0 = 1.0$ and 8.0. The bottom layers in (b) are out of focus due to the expansion. From the recorded videos, the time-averaged velocity fields are obtained by PIV (Particle Image Velocimetry). The resulting shear profile v/v_p is plotted against z/d for different γ_0 in fig. 3(c), where v_p is the plate velocity and z is the depth into the suspension, measured from the top. Before the onset of shear thickening, a shear band near the top plate is observed, extending a distance d_s. As γ_0 increases, the band gradually expands until spanning the entire gap ($d_s \sim d$ at $\gamma_0 \gtrsim 0.5$). With continuing increase of γ_0, particles near the bottom are pushed out and form effectively static layers that no longer participate in shear ($\gamma_0 = 3.2$ and 10.0).

Result analysis. – In order to understand the evolution of the shear profile shown in fig. 3(c) quantitatively, a microscopic constitutive relation has to be considered that accounts for the local stresses in the suspension. Quite generally, the shear stress τ_0 contains contributions from hydrodynamic and inter-particle forces that could arise from a variety of sources [2,11]. For dense granular suspensions of hard, non-Brownian particles, the dominant inter-particle forces arise from direct, frictional contact [2–4,9,18]. Thus, given a local, z-dependent shear rate $\dot\gamma_l(z)$,

$$\tau_0 = \eta_h \dot\gamma_l(z) + \tau_g z/d + \tau_c(\dot\gamma_0). \qquad (1)$$

Here, the first term represents the viscous hydrodynamic stress, contributing an amount η_h to the measured overall viscosity, while the shear-rate–independent remainder reflects the inter-particle forces. We have split this remainder into two parts to separate out the frictional stresses originating from sedimentation (τ_g) due to gravity and frictional contacts (τ_c) due to shear [18].

The second term in eq. (1) scales linearly with z due to gravity. To move the particles at the bottom layer ($z = d$), the required stress is at least τ_g. In a suspension of hard non-Brownian particles, $\tau_g = \mu_c \Delta\rho g d/15.3$, where μ_c is the friction coefficient (~ 0.8 for ZrO_2), and gives the magnitude of the onset stress for our system [18]. The last term in eq. (1), τ_c, is written as a function of the global shear rate $\dot\gamma_0 (= \omega\gamma_0)$ but is independent of the local quantity $\dot\gamma_l$. Therefore, by integrating $\dot\gamma_l$ over z, we obtain the velocity profile:

$$\frac{v}{v_p} = \frac{\tau_g}{2\omega\gamma_0\eta_h}\left(\frac{d_s - z}{d}\right)^2 \qquad (d_s < d), \qquad (2)$$

$$\frac{v}{v_p} = \frac{(\tau_0 - \tau_g - \omega\gamma_0\eta_c)(d - z)}{\omega\gamma_0\eta_h d} + \frac{\tau_g}{2\omega\gamma_0\eta_h}\left(\frac{d - z}{d}\right)^2 \qquad (d_s > d). \qquad (3)$$

Here, $d_s = (\tau_0 - \tau_c)d/\tau_g$ is the depth of the sheared layers and $\eta_c = \tau_c/(\omega\gamma_0)$ indicates the contribution to the viscosity caused by dilation against confining boundaries. Equation (2) thus corresponds to shear banding and

[1] Inertia is a negligible factor in this case since the Stokes number $St \approx 0.04 \ll 1$.

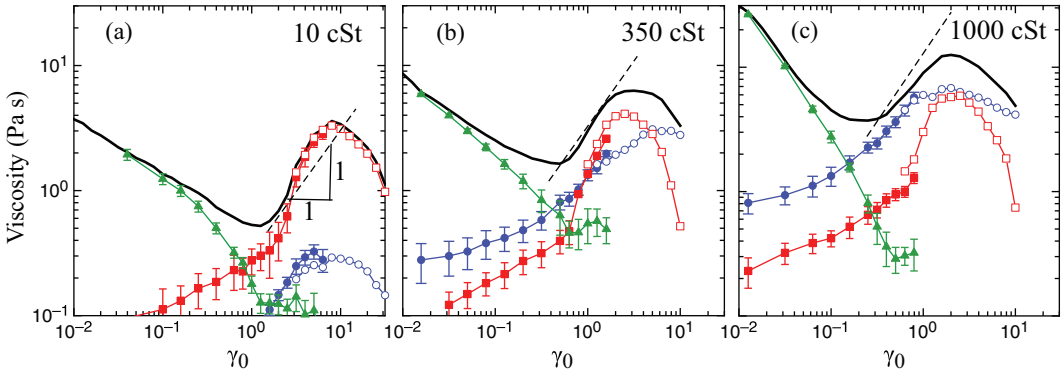

Fig. 4: (Color online) The viscosity components due to hydrodynamics (η_h), dilation (η_c) and sedimentation (η_g) in the rheological measurement. While the black lines is the measured viscosity $|\eta^\star|$ recorded by the rheometer, η_h, η_c and η_g are plotted in blue, red and green, respectively. The solid data points are obtained by the fit to eqs. (2) and (3). The open symbols correspond to the large-strain regime, where we directly calculate $\tau_c = \mu_c \tau_{N0}$ and $\eta_h = |\eta^\star| - \eta_c$. The suspending viscosities were varied to be (a) 10 cSt, (b) 350 cSt and (c) 1000 cSt. The dashed lines indicate the Bagnoldian scaling: $|\eta^\star| \sim \gamma_0$.

eq. (3) to fully developed shear flow within the effective gap region (which can become smaller than d once the contact line moves out).

When $\gamma_0 \leq \gamma_c \approx 0.5$, the applied stress $\tau_0 \leq 0.76$ Pa (see fig. 3(d)) is so small that $d_s < d$ and eq. (2) predicts parabolic shear profiles. Beyond the thickening onset ($\gamma_0 > \gamma_c \approx 0.5$), $\tau_0 > \tau_g$ and therefore $d_s > d$, corresponding to global motion across the entire suspension, such that the shear profile is governed by eq. (3) containing both linear and parabolic terms.

As $\gamma_0 > 2$, the sedimentation contribution (τ_g) becomes negligible compared to the other terms in eq. (1). Accordingly, eq. (3) simplifies to a linear profile $v/v_p \approx (\tau_0 - \tau_c)z/(\omega\gamma_0\eta_h d_{eff})$, where d_{eff} is the effective gap height, *i.e.*, the depth at which $v(z) = 0$. In the absence of wall slip (see velocity profiles in fig. 3(c)), the slope of v/v_p plotted against z/d_{eff} has to be equal to unity. Writing τ_0 and τ_c in terms of the associated viscosity contributions, this leads to

$$\eta_h + \eta_c = |\eta^\star|. \tag{4}$$

In principle, the values of η_h and η_c can be obtained by fitting the profile data to eqs. (2) and (3), or for linear profiles, to eq. (4). However, eq. (4) is not sufficient to extract the values of both η_h and η_c. To resolve this problem, we assume that the normal stress in this regime is purely frictional such that $\tau_c \approx \mu_c \tau_{N0}$ [18,26], where τ_{N0} is the measured normal stress amplitude (see fig. 3(d)), and $\eta_c = \mu_c \tau_{N0}/(\omega\gamma_0)$. Thus, in the large-strain regime, we calculate $\eta_h = |\eta^\star| - \mu_c\tau_{N0}/(\omega\gamma_0)$ from eq. (4).

Based on the values of η_h and η_c at different strain amplitudes, we can assemble a diagram to indicate the contribution from different viscosity components to $|\eta^\star|$. Figure 4(b) sums up the results for the ZrO_2 beads in 350 cSt silicone oil. The black line shows $|\eta^\star|$ *vs.* γ_0 from fig. 1. On the same plot, the blue circles and red squares represent the magnitudes of η_h and η_c, respectively. While the solid points are from the fits to eqs. (2) and (3), open symbols correspond to the regime at large strain amplitudes when the shear profile is close to linear and the values of η_h and η_c are from eq. (4) together with $\eta_c = \mu_c\tau_{N0}/(\omega\gamma_0)$. As we compare the two procedures within the same range of $1.0 < \gamma_0 < 2.0$, the results from the fit and calculation consistently follow the same trend in the plot, suggesting that the assumption of frictional contacts and $\tau_c \approx \mu_c\tau_{N0}$ is reasonable. As shown in fig. 4(b), the increase of η_c is in general steeper than η_h. During the ST transition ($0.5 < \gamma_0 < 4.0$), the ratio of η_c and η_h reaches a factor up to two, indicating that dilation is still a more important factor to shear thickening than the increase of hydrodynamic interactions.

In addition, we define $\eta_g = |\eta^\star| - \eta_c - \eta_h$ as the viscosity component due to sedimentation. Considering eq. (1), η_g can be written as

$$\eta_g = \eta_h \left[\left| \frac{\mathrm{d}(v/v_p)}{\mathrm{d}(z/d)} \right|_{z=0} - 1 \right]. \tag{5}$$

This term is determined by the slope of the shear profile near the top plate ($z = 0$). In the presence of sedimentation, the shear profiles are non-linear. For very small γ_0, the velocity gradient is significant at $z = 0$ since the shear flow is localized within a very small layer of the suspension near the top plate. Therefore, η_g is sufficiently large to be dominant in this regime (green triangles). As γ_0 increases, the flow region expands and the shear profile becomes less steep, such that η_g decreases and the system shear-thins until dilation and hydrodynamic effects set in.

Panels (a) and (c) in fig. 4 show the behavior if the suspending oil viscosity is changed. The shear thinning regime is always dominated by η_g. Shear thickening, however, is determined by both η_c and η_h. While η_c remains roughly the same, η_h changes substantially when varying the suspending liquid viscosity from 10 to 1000 cSt. For 10 cSt oil (fig. 4(a)), $\eta_c \gg \eta_h$, which explains why ST in this regime can be described by frustrated dilation alone [4,8,18]. For 1000 cSt oil, on the other hand, η_h has increased about two orders of magnitude and we

have $\eta_h > \eta_c$ for the entire measurement range. Thus, in the highly viscous regime, hydrodynamics starts to play an important role in controlling ST.

Specifically, the increase in η_h affects the steepness of the flow curve and softens the discontinuous nature of ST. For 10 cSt oil (fig. 4(a)), the slope in ST regime is steeper than the dashed lines, which represent the classical Bagnoldian scaling, $|\eta^\star| \sim \gamma_0$ [7,9]. While increasing the oil viscosity to 1000 cSt (fig. 4(c)), for instance, ST is found to be weaker than the Bagnoldian scaling since η_h becomes crucial but increases in a way less steep than η_c.

In the discussion above, even though we separate the measured viscosity into different factors, hydrodynamics (η_h), dilation (η_c) and sedimentation (η_g), it is important to realize that the frictional and viscous forces that contribute to these three components are mutually coupled [3,4]. Equation (5), for example, shows that the rheology associated with sedimentation (η_g) is coupled with viscous interactions (η_h) while the shear profile is non-linear. Besides that, from inspecting the data of η_c in fig. 4, one can tell that, with the increase of solvent viscosity, the difference between the experimental data (red solid points) and direct calculation (red hollow data) becomes discernible. It suggests that the effective frictional coefficient between particles becomes smaller. Thus, strictly speaking, the effective frictional coefficient μ_c depends on η_0.

Discussion. – To track more systematically the effect of increasing the hydrodynamic contributions, we plot the ratio of η_h to η_c at the upper bound of the ST regime (where $|\eta^\star|$ reaches the maximum), $(\eta_h/\eta_c)|_{max}$, against the suspending oil viscosity, η_0, in fig. 5. While varying the particle size a from 125 to 300 μm, the curves remain of the same shape. This independence from the particle size can be qualitatively explained as follows. The maximum dilational stress is balanced by the Laplace pressure over the local menisci at the suspension-air interface, and thus $\tau_c|_{max}$ approximately scales as $1/a$ [16]. Since the maximum strain amplitude within the ST regime, $\gamma_0|_{max}$, is also found to scale as $1/a$ (see fig. 5(b)), $\eta_c|_{max} = (\tau_c/\omega\gamma_0)|_{max}$ is independent of a. On the other hand, if the hydrodynamic viscosity is mainly due to lubrication, $\eta_h \sim \eta_0 a/\delta$, where δ is the inter-particle distance [12,27]. For a fully developed thickening flow, a/δ is a function of the packing fraction, such that η_h is also independent of a. As a result, $(\eta_h/\eta_c)|_{max}$ does not vary with the particle size.

Physically, the plot in fig. 5 shows a crossover from a granular regime, where η_c dominates the viscosity, to a hydrodynamic regime when η_h dominates. Near $\eta_h \sim \eta_c$, the suspensions exhibit both granular and hydrodynamic characters.

Conclusions. – Under oscillatory shear, the ST onset in dense granular suspensions can be characterized by a critical strain γ_c (fig. 1) that signals the onset of dilation against a confining interface. ST sets in as particles begin to protrude through the interface and stops when the contact line between suspension and substrate starts to move, reflecting that the maximum confining stress has been reached (fig. 2). Modeling the shear flow by a local constitutive relation, we quantified the contributions from different sources to the measured viscosity (figs. 3 and 4). With increasing viscosity of the suspending liquid, the hydrodynamic contributions can become sufficiently large so that they compete with the effects from frustrated dilation (fig. 5) and soften the discontinuous nature of ST in dense granular suspensions.

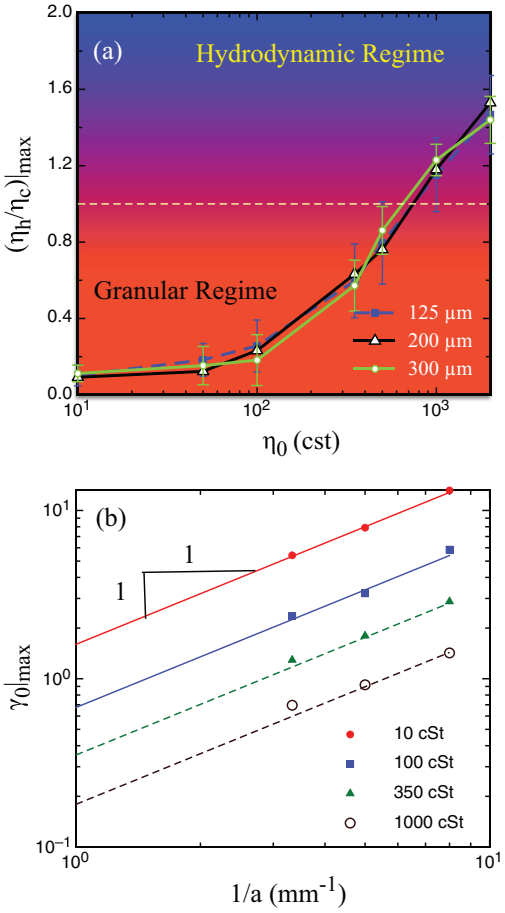

Fig. 5: (Color online) (a) Ratio of viscosity components due to hydrodynamics and confinement, η_h and η_c, at the upper bound of the shear thickening regime, $(\eta_h/\eta_c)|_{max}$, *vs.* viscosity of the suspending oil, η_0, for ZrO_2 suspensions. Error bars come from the standard deviation of four individual runs of measurement. The particle size is varied from 125 to 300 μm. The dashed line represents $\eta_c = \eta_h$. (b) Maximum strain, $\gamma_0|_{max}$, *vs.* the inverse of the particle size, $1/a$, for different suspending viscosities.

* * *

We thank Ivo R. Peters and Carlos S. Orellana for many discussions. This work was supported by the U.S. Army Research Office through Grant No. W911NF-12-1-0182 and by the National Science Foundation (NSF) MRSEC program under Grant No. DMR-0820054.

EB acknowledges support from NSF-DMR-1410157. SM acknowledgs the support from a Kadanoff-Rice Postdoctoral Fellowship.

REFERENCES

[1] Barnes H. A., *J. Rheol.*, **33** (1989) 29.
[2] Brown E. and Jaeger H. M., *Rep. Prog. Phys.*, **77** (2014) 046602.
[3] Mari R., Seto R., Morris J. F. and Denn M. M., arXiv:1403.6793 (2014).
[4] Seto R., Mari R., Morris J. F. and Denn M. M., *Phys. Rev. Lett.*, **111** (2013) 218301.
[5] Wyart M. and Cates M. E., *Phys. Rev. Lett.*, **112** (2014) 098302.
[6] Cates M. E., Wittmer J. P., Bouchaud J.-P. and Claudin P., *Phys. Rev. Lett.*, **81** (1998) 1841.
[7] Fall A., Lemaître A., Bertrand F., Bonn D. and Ovarlez G., *Phys. Rev. Lett.*, **105** (2010) 268303.
[8] Heussinger C., *Phys. Rev. E*, **88** (2013) 050201(R).
[9] Fernandez N., Mani R., Rinaldi D., Kadau D., Mosquet M., Burger H. L., Barrioz J. C., Herrmann H. J., Spencer N. D. and Isa L., *Phys. Rev. Lett.*, **111** (2013) 108301.
[10] Chu C. E., Groman J. A., Sieber H. L., Miller J. G., Okamoto R. J. and Katz J. I., arXiv:1405.7233 (2014).
[11] Maranzano B. J. and Wagner N. J., *J. Chem. Phys.*, **114** (2001) 10514.
[12] Wagner N. J. and Brady J. F., *Phys. Today*, **62**, issue No. 10 (2009) 27.
[13] Brady J. F. and Bossis G., *J. Fluid Mech.*, **155** (1985) 105.
[14] Cheng X., McCoy J. H., Israelachvili J. N. and Cohen I., *Science*, **333** (2011) 1276.
[15] Brown E., Forman N. A., Orellana C. S., Zhang H., Maynor B. W., Betts D. E., DeSimone J. M. and Jaeger H. M., *Nat. Mater.*, **9** (2010) 220.
[16] Brown E. and Jaeger H. M., *Phys. Rev. Lett.*, **103** (2009) 086001.
[17] Holmes C. B., Cates M. E., Fuchs M. and Sollich P., *J. Rheol.*, **49** (2005) 237.
[18] Brown E. and Jaeger H. M., *J. Rheol.*, **56** (2012) 857.
[19] Fall A., Huang N., Bertrand F., Ovarlez G. and Bonn D., *Phys. Rev. Lett.*, **100** (2008) 018301.
[20] Wilhelm M., Reinheimer P., Ortseifer M., Neidhöfer T. and Spiess H., *Rheol. Acta*, **39** (2000) 241.
[21] Ewoldt R. H., Hosoi A. E. and McKinley G. H., *J. Rheol.*, **52** (2008) 1427.
[22] Koumakis N., Pamvouxoglou A., Poulos A. S. and Petekidis G., *Soft Matter*, **8** (2012) 4271.
[23] Fall A., Bertrand F., Ovarlez G. and Bonn D., *J. Rheol.*, **56** (2012) 575.
[24] Lee Y. S. and Wagner N. J., *Rheol. Acta*, **42** (2003) 199.
[25] Brown E., Zhang H., Forman N. A., Maynor B. W., Betts D. E., DeSimone J. M. and Jaeger H. M., *J. Rheol.*, **54** (2010) 1023.
[26] Rognon P., Einav I. and Gay C., *J. Fluid Mech.*, **689** (2011) 77.
[27] Marshall J. S., *Phys. Fluids*, **23** (2011) 013305.